Exploiting finite size effects in a novel core/shell microstructure

Zhu Liu,[1] Guoqiang Xia,[2] Frank Zhu,[2] Su Kim,[1] Nina Markovic,[2] Chia-Ling Chien,[1,2] and Peter C. Searson[1,2,a)]
[1]*Department of Materials Science and Engineering, Johns Hopkins University, Baltimore, Maryland 21218, USA*
[2]*Department of Physics and Astronomy, Johns Hopkins University, Baltimore, Maryland 21218, USA*

(Received 11 May 2007; accepted 15 December 2007; published online 24 March 2008)

Electrodeposition of Ni–Cu alloys at high Cu(II) concentration and large overpotentials results in phase separation with a unique microstructure characterized by features with a copper-rich core and a nickel-rich shell. By confining deposition to nanoporous channels with dimensions comparable to or smaller than the grain size results in the formation of solid Ni–Cu nanowires with a copper-rich core and a nickel-rich shell. Etching of the copper-rich core results in the formation of Ni-rich nanotubes. The magnetic properties of the Ni–Cu nanowires and the Ni nanotubes are investigated.
 [DOI: 10.1063/1.2844286]

INTRODUCTION

The ability to control the architecture of magnetic structures at the nanoscale has resulted in the discovery of new magnetic properties and novel devices. Structures such as nanocylinders,[1] nanowires,[2] nanotubes,[3] and nanorings[4] have been produced by template synthesis and lithography. The cylindrical ring and tube geometries are of particular interest due to the fact that the magnetic flux is confined within the structure and hence there are no stray fields.

Here, we report on a unique core/shell microstructure observed in electrodeposited Ni–Cu alloys. We demonstrate that by confining nucleation in a template, the core/shell microstructure can be exploited in the fabrication of ferromagnetic nanorings and nanotubes, as illustrated schematically in Fig. 1.

The difference in equilibrium potentials for Ni and Cu is quite large, making it possible to electrochemically deposit both alloys[5,6] and multilayer structures[7–12] from a single solution containing both copper and nickel ions. Nickel and copper are both fcc and have similar lattice parameters, suggesting complete solid solubility across the whole compositional range; however, recent calculations have shown a miscibility gap at temperatures below 600 K.[13,14] The miscibility gap provides the thermodynamic driving force for phase separation and leads to the core/shell microstructure.

EXPERIMENTAL SECTION

Ni–Cu alloy thin films were electrodeposited from solution containing 0.4*M* $Ni(H_2NSO_3)_2 \cdot 4H_2O$ (99.99% Aldrich), 5–100 mM $CuSO_4 \cdot 5H_2O$ (98%, Aldrich), and 0.65*M* HBO_3 (Alfa Aesar) at a *p*H of 3.8. A Au (111) thin film sputtered on Si (111) served as a working electrode in a three electrode cell with a platinum mesh (99%, Sigma Aldrich) counterelectrode and a Ag/AgCl (3*M* NaCl) reference electrode (Bioanalytical Systems). All potentials are reported versus the Ag/AgCl reference (U_{eq}=0.200 V versus standard hydrogen electrode). In all cases the deposition charge was 3 C cm^{-2} corresponding to a film thickness of about 1 μm [assuming a deposition efficiency of 0.95 (Ref. 5)]. Etching of the Cu-rich phase from the two phase alloys was performed at 0.5 V for 20 min in the same solution.

Ni–Cu alloy nanowires were electrodeposited into polycarbonate templates (Osmonics) with nominal pore diameters of 30, 100, and 220 nm, from solution containing 0.4*M* $Ni(H_2NSO_3)_2 \cdot 4H_2O$, 0.05*M* $CuSO_4 \cdot 5H_2O$, and 0.65*M* HBO_3. A 700 nm thick gold layer was sputtered onto one side of template at 5 mTorr as a working electrode for deposition. In all cases the deposition charge was 1 C cm^{-2}, resulting in alloy nanowires about 3.3 μm long. For scanning electron microscopy (SEM) characterization the nanowires were stripped from the template. First, the sputtered gold layer on the polycarbonate template was removed by contacting with mercury. The template was then immersed in chloroform (Alfa Aesar) to dissolve the polycarbonate and release the nanowires. The nanowires were rinsed sequentially in acetone, ethanol, and de-ionized water, and then stored in ethanol or de-ionized water.

The magnetization of the nickel nanotubes was compared to nickel nanowires. The nickel nanowires were deposited at −1.0 V in polycarbonate templates with 220 nm diameter pores from solution containing 0.4*M* $Ni(H_2NSO_3)_2 \cdot 4H_2O$ and 0.65*M* HBO_3. The deposition charge was 1 C cm^{-2}. The total saturation magnetization, determined from vibrating sample magnetometer measurements, was about 17 memu cm^{-2}. From SEM images we determined an average length of 3.3 μm. From the average length and taking a pore density of 2.5×10^8 cm^{-2}, this cor-

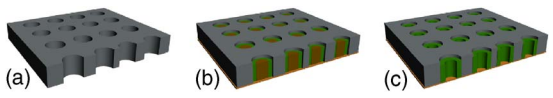

FIG. 1. (Color online) Schematic illustration of the process for fabrication of nickel nanotubes: (a) nanoporous template, (b) electrodeposition of core/shell nanowires with a nonmagnetic (Cu-rich) core and a ferromagnetic (Ni-rich) shell, and (c) etching of the nonmagnetic core results in the formation of a ferromagnetic nanotube.

a)Electronic mail: searson@jhu.edu.

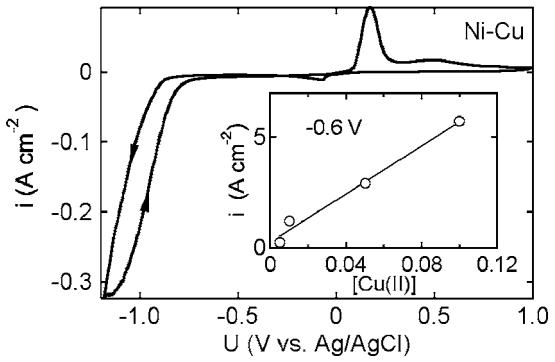

FIG. 2. Current-voltage curve for gold in solution containing 5 mM Cu(II) and 400 mM Ni(II). The scan rate was 20 mV s^{-1}. The inset shows the diffusion limited deposition current at −0.6 V vs the Cu(II) concentration in solution.

responds to a magnetization of 460 emu cm^{-3}, close to the value for bulk nickel of 490 emu cm^{-3} and indicating that the efficiency of Ni deposition is about 0.95.

The structure and composition of thin films and nanowires were determined by x-ray diffraction (Phillip's X Pert 3040) with a Cu $K\alpha$ source. The surface morphology was characterized by SEM (JEOL 6700F). Magnetization hysteresis loops of arrays of Ni–Cu nanowires before and after dealloying were measured at room temperature using a vibrating sample magnetometer (Vector, model 10).

Micromagnetic simulations of ferromagnetic nanotubes were performed using the OOMMF software package (NIST). The relevant parameters used for nickel in the simulations were a saturation magnetization, $M_S = 4.9 \times 10^5$ A m^{-1}, and an exchange stiffness, $A = 1.3 \times 10^{-11}$ J m^{-1}. The cell size was $10 \times 10 \times 20$ nm^3 in the x, y, and z directions, respectively. All simulations were performed for tubes with an outer diameter of 220 nm, a wall thickness of 40 nm, and a length of 3.3 μm.

RESULTS AND DISCUSSION

Thin films

Thin films were deposited from solution with 400 mM Ni(II) and 5–100 mM Cu(II), corresponding to Ni(II)/Cu(II) ratios of 4–80. Figure 2 shows a current-voltage curve for gold in solution containing 400 mM Ni(II) and 5 mM Cu(II). As the potential is scanned from the open circuit potential (about 0.34 V) to more negative potentials, the onset of copper deposition is seen at potentials very close to the equilibrium potential for the Cu^{2+}/Cu couple [U_{eq} = −0.07 V for 5 mM Cu(II)]. The onset of nickel deposition occurs at about −0.70 V, more than 0.22 V negative of the equilibrium potential for the Ni^{2+}/Ni couple [U_{eq} = −0.48 V for 400 mM Ni(II)]. At potentials negative to −0.70 V, nickel and copper depositions occur simultaneously. On scanning the potential in the positive direction, a peak is seen at potentials positive to the copper equilibrium potential corresponding to dissolution of copper. In this solution nickel is passivated and hence only copper is selectively etched from the alloy.[5,11]

The relative rates of deposition of copper and nickel are dependent on the applied potential and ion concentrations. In

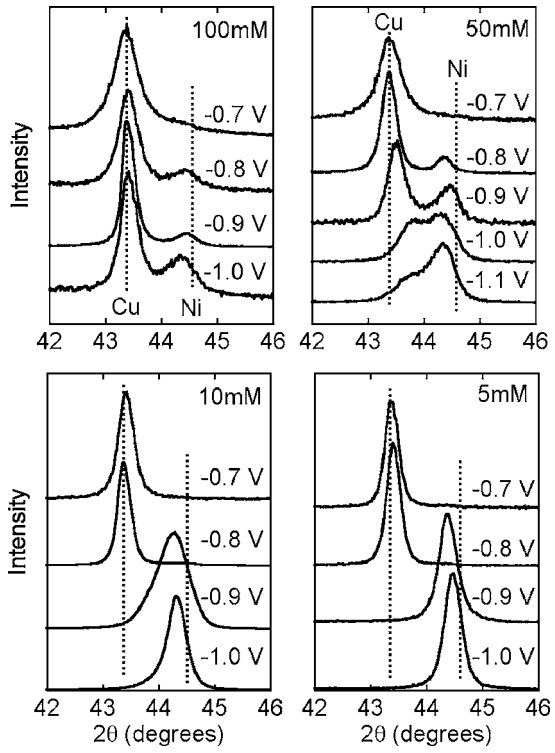

FIG. 3. X-ray diffraction patterns for Cu–Ni thin films deposited from solution containing 5–100 mM Cu(II) and 400 mM Ni(II) as a function of deposition potential. In all cases the deposition charge was 3 C cm^{-2} corresponding to a film thickness of about 1 μm.

the potential range from −0.7 to −1.1 V, where Ni–Cu alloys were deposited, Cu deposition is diffusion limited and hence the deposition rate is expected to be proportional to the Cu(II) concentration but independent of applied potential, as shown in Fig. 2. Since the rate of nickel deposition increases with increasing overpotential, the composition of electrodeposited alloys becomes more Ni-rich as the potential becomes more negative.

Figure 3 shows x-ray diffraction patterns for Ni–Cu thin films deposited at different Cu(II) concentrations. The diffraction patterns are centered around the Cu(111) and Ni(111) peaks located at 43.41° and 44.59°, respectively.[15] At low Cu(II) concentrations (5 and 10 mM), the diffraction patterns show a single peak corresponding to the deposition of a single phase solid solution over the potential range from −0.7 to −1.0 V. At higher Cu(II) concentrations (50 and 100 mM) a single peak indicating a single phase solid solution is observed at −0.7 V. However, for deposition potentials from −0.8 to −1.0 V the diffraction patterns show two peaks, corresponding to the formation of a two phase alloy with Ni-rich and Cu-rich phases. With more negative deposition potentials, the peak corresponding to the Ni-rich phase increases in intensity, and the peak corresponding to the copper-rich phase decreases in intensity. This is consistent with the fact that the rate of nickel deposition increases at more negative potentials, whereas the rate of copper deposition remains essentially constant. Comparison of the diffraction peaks for 50 and 100 mM Cu(II) shows that with increasing Cu(II) concentration in solution, the fraction of the Cu-rich phase at any deposition potential increases, as evi-

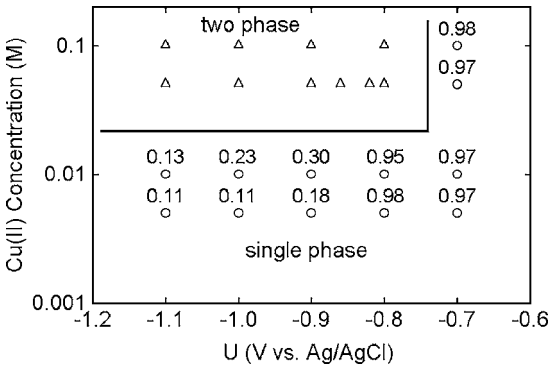

FIG. 4. Phase diagram indicating single-phase and two-phase regimes for Ni–Cu thin films deposited from solution containing 5–100 mM Cu(II) and 400 mM Ni(II). The mole fraction of copper in the single phase alloys is indicated above each point.

denced by the increase in the intensity of the peak corresponding to the Cu-rich phase relative to the intensity of the peak corresponding to the Ni-rich phase.

A unique feature of the films deposited from 50 mM Cu(II) solution is that the separation $\Delta 2\theta$ between the Cu-rich peak and the Ni-rich peak decreases with more negative deposition potentials. In contrast, the peak separation for films deposited from 100 mM Cu(II) solution appears independent of deposition potential.

The influence of Cu(II) concentration and deposition potential on phase separation is summarized in Fig. 4. At higher Cu(II) concentrations, where $\mathrm{Ni(II)/Cu(II)} \leqslant 8$, phase separation is seen at potentials $\leqslant -0.8$ V. At lower Cu(II) concentrations, however, where $\mathrm{Ni(II)/Cu(II)} > 8$, a single phase alloy is obtained across the potential range from −0.7 to −1.1 V. A feature of deposition at low Cu(II) concentrations where $\mathrm{Ni(II)/Cu(II)} > 8$ is that the composition does not change monotonically at more negative potentials; there is a large change in composition from $x \geqslant 0.95$ at −0.8 V to $x \leqslant 0.3$ at potentials $\leqslant -0.9$ V. These results show why Cu/Ni multilayers are deposited at high Ni(II)/Cu(II) ratio, where the potential can be modulated from a more positive potential where copper is deposited to a more negative potential, typically about −1.0 V, where a nickel-rich alloy is deposited.[8,11,12]

Thin films deposited under conditions where phase separation is observed exhibit a unique core/shell columnar microstructure. Figure 5(a) shows a SEM image of a film deposited at −0.9 V, revealing a nodular microstructure. Selective electrochemical etching of the copper results in an array of cylindrical pores over the surface, as shown in Fig. 5(b). Copper is more noble than nickel, and hence preferential etching of copper is not possible thermodynamically. However, in sulfamate solutions nickel forms a thin oxide layer that effectively passivates the surface, allowing copper to be selectively etched.[11] SEM images of the back side and cross-sectional images (not shown) confirm that the pores are relatively uniform cylinders extending through the film. Analysis of the pores in the etched film at −0.9 V [Fig. 5(b)] reveals a Gaussian distribution with a near neighbor distance of 240 ± 54 nm [Fig. 5(c)], in excellent agreement with the near neighbor distance of 230 ± 59 nm obtained from analysis of the nodular features [Fig. 5(a)]. Since the pores are derived from the copper-rich phase, it is clear that the microstructure is characterized by a columnar core/shell structure with a copper-rich core and surrounding nickel-rich shell.

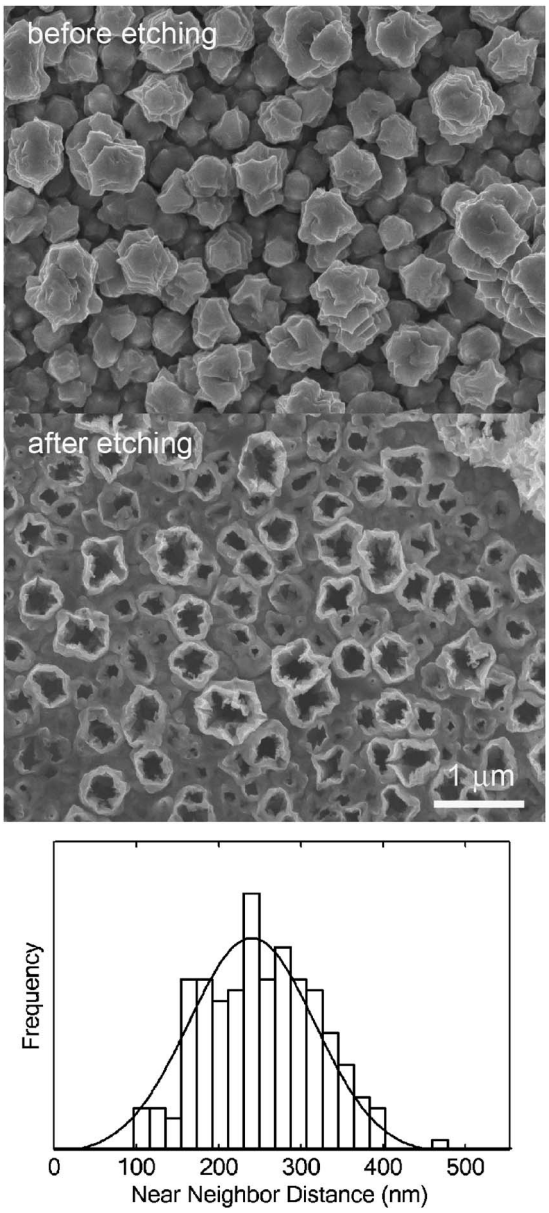

FIG. 5. Plan view SEM images (a) before and (b) after etching a Ni–Cu thin film deposited at −0.9 V from solution containing 50 mM Cu(II) and 400 mM Ni(II). (c) Near neighbor distribution obtained from the center of the channels formed in the nodular features after etching.

The experiments described above were performed on a relatively large surface area with a large number of core/shell features. These results suggest that by reducing the deposition area to dimensions comparable to or smaller than the average feature size, it would be possible to deposit single core/shell nanowires with a Ni-rich shell and a Cu-rich core. Furthermore, etching the copper core from the nanowires can be used to fabricate nickel rings and tubes.

Nanotubes

To investigate the influence of confined geometry on deposition, we have deposited Ni–Cu alloys into templates

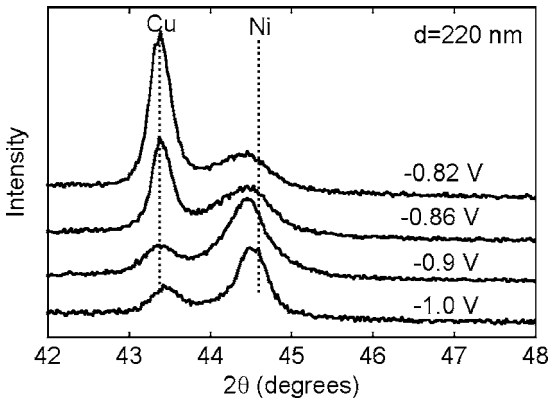

FIG. 6. X-ray diffraction patterns for Ni–Cu nanowires deposited from solution containing 50 mM Cu(II) and 400 mM Ni(II) in templates with a nominal pore diameter of 220 nm.

with 220 nm cylindrical pores. Figure 6 shows x-ray diffraction patterns for Ni–Cu nanowires deposited into templates with 220 nm diameter pores from solution containing 50 mM Cu(II) at −0.82, −0.86, −0.9, and −1.0 V. The diffraction patterns show two peaks corresponding to a Ni-rich phase and a Cu-rich phase. In contrast to the thin films, however, the separation between the two peaks remains large at all deposition potentials.

Figure 7 shows x-ray diffraction patterns for Ni–Cu nanowires deposited at −1.0 V from solution containing 50 mM Cu(II) before and after etching the copper. Before etching, the diffraction pattern shows both a Cu-rich phase and a Ni-rich phase. After etching, the peak corresponding to the Cu-rich phase disappears, indicating that the Cu-rich phase is completely removed from the nanowires. The small shift in the Ni-rich peak to a smaller angle is likely due to stress release after etching.[12]

Figure 8 shows SEM images of Ni–Cu nanowires after etching the copper, illustrating that the nickel-rich phase remaining after etching forms nanotubes. Although the outer walls of the nanotubes appear somewhat rough, the images show that the wall thickness slightly increases with more negative deposition potentials, as would be expected for an increase in the rate of nickel deposition.

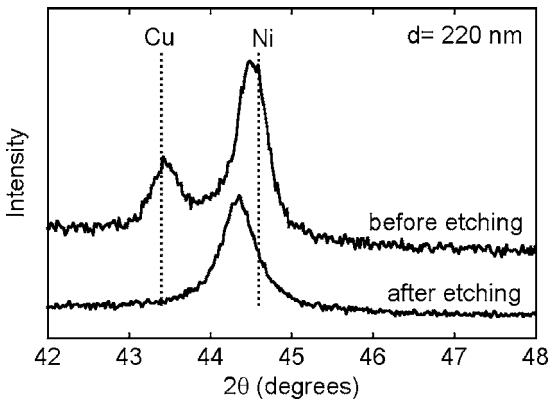

FIG. 7. X-ray diffraction patterns for Ni–Cu nanowires deposited at −1.0 V from solution with 50 mM Cu(II) and 400 mM Ni(II) before and after etching.

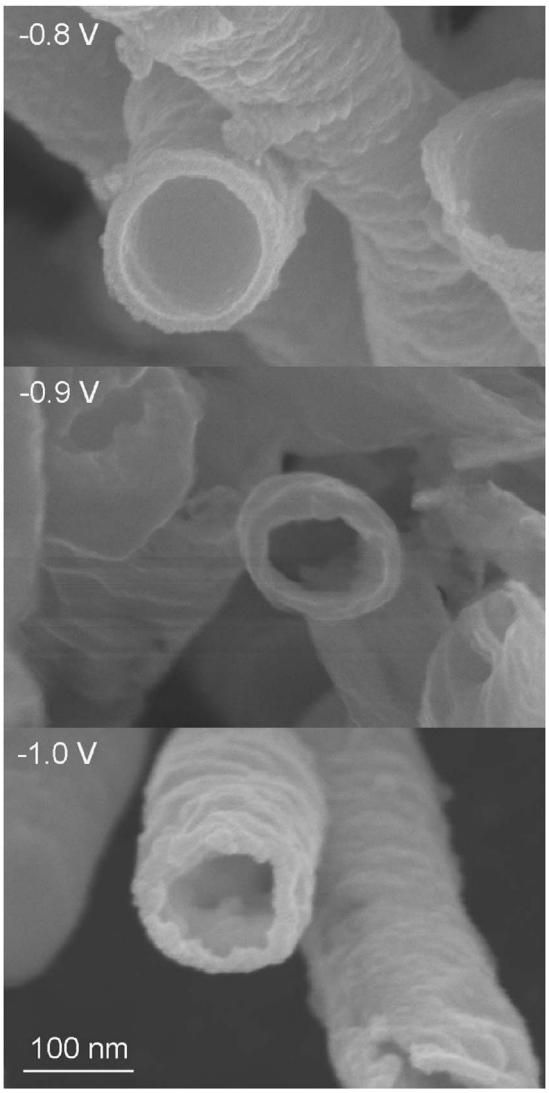

FIG. 8. SEM images of the Ni nanotubes formed by etching Ni–Cu alloy nanowires deposited at (a) −0.8 V, (b) −0.9 V, and (c) −1.0 V from solution containing 50 mM Cu(II) and 400 mM Ni(II).

As described above, confinement of nucleation and growth leads to the formation of single features with a cylindrical core/shell structure. Figure 9 shows the influence of pore diameter on phase separation and the formation of the core/shell structure. Cu–Ni nanowires were deposited at −1.0 V from solution containing 50 mM Cu(II). The diffraction pattern for Ni–Cu nanowires in 100 nm diameter pores is very similar to the diffraction pattern in 220 nm diameter pores with a Cu-rich phase and a Ni-rich phase. However, when the pore diameter is decreased to 30 nm, a single broad Ni-rich peak is observed. This result shows that confinement of the deposition area only results in the formation of single core/shell nanowires over a limited range. For the experiments reported here, single core/shell nanowires were obtained with pore diameters of 100–220 nm.

To understand the Ni–Cu phase separation and the formation of core/shell structures, we propose a model illustrated in Fig. 10. As shown in the phase diagram in Fig. 4, the two phase region is located at high Cu (II) concentrations and more negative deposition potentials. In this regime, the

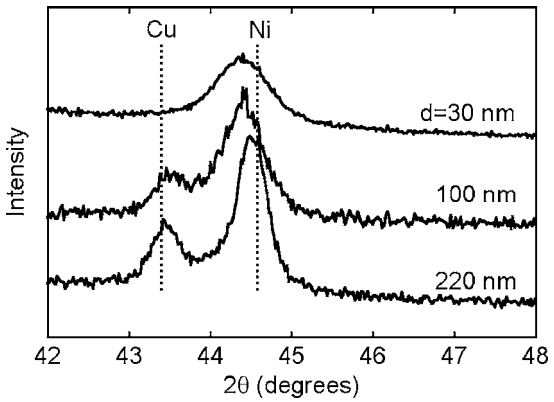

FIG. 9. X-ray diffraction patterns for Ni–Cu alloy nanowires deposited at −1.0 V from solution containing 50 mM Cu(II) and 400 mM Ni(II) into templates with nominal pore diameters of 30, 100, and 220 nm.

Cu nucleation rate is much faster than the nucleation rate for Ni, resulting in the formation of copper islands during the early stages of deposition. As the surface becomes depleted of Cu(II) ions due to the growth of the copper islands, nickel nucleation is enhanced in the regions surrounding the copper islands. Separation between the two phases during subsequent growth is consistent with the miscibility gap,[13,14] leading to the characteristic core/shell microstructure.

The SEM images of the nanotubes in Fig. 8 imply the nucleation of a single Cu-rich island at the bottom of the cylindrical pore in the template. For the Cu-rich core to be centered in the core/shell structure, the Cu islands must be nucleated at the center of the pore base, or if the Cu island is randomly nucleated, then it must quickly become centered during the early stages of growth. In the latter case, differences in the diffusive transport of Cu(II) ions to the growing island could provide an explanation. Due to volume exclusion, the flux of ions will be lower at a point on a hemispherical island that is closer to the sidewall. The characteristic columnar microstructure ensures that the copper core is surrounded by nickel in a core/shell structure, as inferred from the SEM images in Fig. 5.

Magnetic properties

Figure 11 shows the saturation magnetization for the

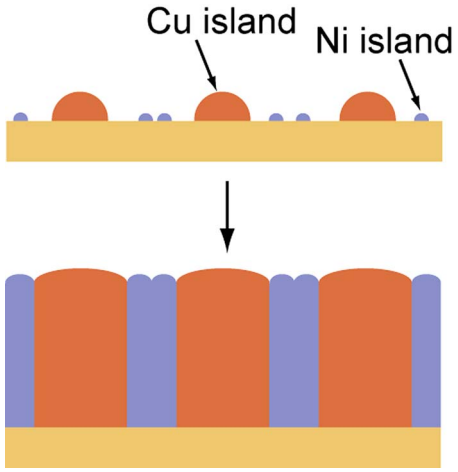

FIG. 10. (Color online) Schematic illustration of phase separation during electrodeposition of Ni–Cu alloys.

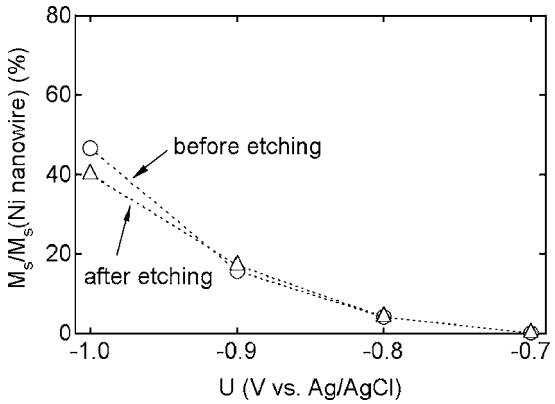

FIG. 11. Normalized saturation magnetization for 220 nm diameter Ni–Cu alloy nanowires deposited from solution containing 50 mM Cu(II) and 400 mM Ni(II) vs deposition potential before and after Cu etching.

Ni–Cu core/shell nanowires before and after etching, normalized to the saturation magnetization for solid Ni nanowires with the same length and diameter. The increase in $M_s(\mathrm{Ni-Cu})/M_s(\mathrm{Ni})$ with more negative deposition potentials illustrates that the fraction of the Ni-rich phase becomes larger. Since the deposition charge and hence nanowire length are constant, this illustrates that the wall thickness of the Ni-rich shell increases with decreasing potential. After etching, the saturation magnetization of the Ni-rich nanotubes decreases very slightly due to the small amount of nickel in the Cu-rich phase. From the saturation magnetization and the nanowire length of 3.3 μm, we determine the wall thicknesses for the Ni-rich phase of 21, 43, and 66 nm at deposition potentials of −0.8, −0.9, and −1.0 V, respectively.

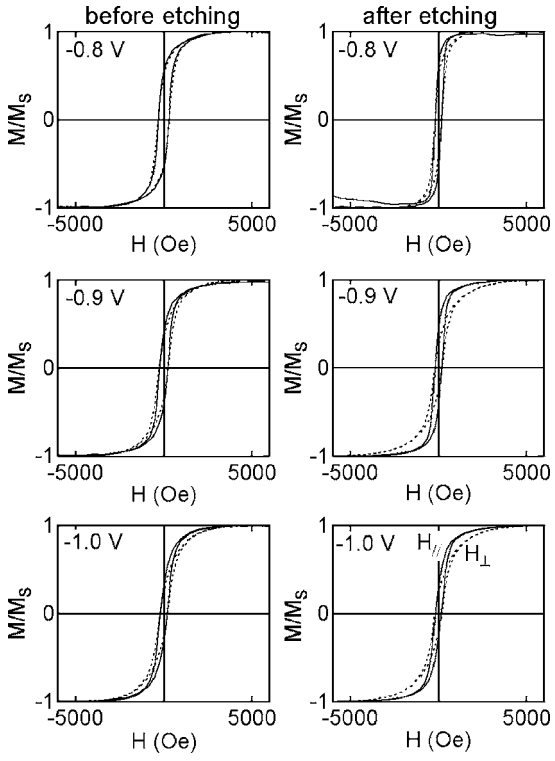

FIG. 12. *M-H* loops for 220 nm diameter Ni–Cu alloy nanowires before and after Cu etching, at deposition potentials of −0.8, −0.9, and −1.0 V. The nanowires were deposited from solution containing 50 mM Cu(II) and 400 mM Ni(II).

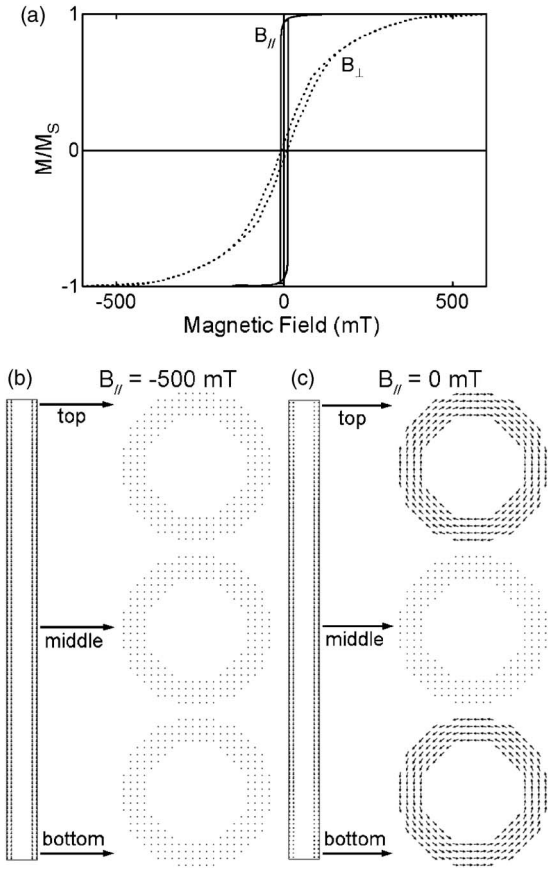

FIG. 13. (a) Simulations of *M-H* loops for a Ni nanotube with a wall thicknesses of 40 nm with the applied fields parallel and perpendicular to the tube axis. The outer diameter was 220 nm and the length was 3.3 μm. Magnetic moments for an applied field parallel to the tube axis of (b) −500 mT and (c) 0 mT.

Figure 12 shows the *M-H* loops for core/shell Ni–Cu nanowires deposited at different potentials, before and after etching the Cu-rich phase. Before etching the hysteresis loops of the core/shell, Ni–Cu nanowires are relatively square and do not exhibit the characteristic shape anisotropy associated with ferromagnetic nanowires of uniform composition.[2,16] After etching the Cu-rich core, the hysteresis loops of the Ni-rich nanotubes parallel to the tube axis are more square and the hysteresis loops perpendicular to the tube axis are more sheared. In addition, the anisotropy of the Ni nanotubes between the two directions becomes more pronounced as the deposition potential becomes more negative, and hence the wall thickness becomes larger.

The *M-H* loops of the Ni nanotubes can be compared to results from micromagnetic simulations. Figure 13 shows simulations of Ni nanotubes with an outer diameter of 220 nm and a wall thickness of 40 nm. Similar results were obtained for wall thicknesses of 20 and 60 nm. The *M-H* loop of Ni nanotubes parallel to the tube axis is relatively square with high remanence. Perpendicular to the tube axis, the *M-H* loop is significantly sheared with low remanence. These features are characteristic of *M-H* loops for single nanotubes. When the tube is magnetized along the tube axis, the magnetizations are aligned parallel to the tube axis. Switching is initiated by rotation of the magnetic moments at the ends of the tube, from parallel to perpendicular to the tube axis, as illustrated in the figure. This process is similar to curling and results in the formation of vortex states with opposite twist at each end of the tube. Similar results have been reported for high aspect ratio nanorings.[17]

The *M-H* loops of the Ni nanotubes shown in Fig. 12 do not exhibit the strong anisotropy characteristic of the simulations. From transmission electron microscopy images (not shown), the average grain size of the nickel is about 20 nm, very close to the wall thickness of the nanotubes (21–66 nm). These results suggest that the microstructure of the tubes influences magnetization through the formation of domain boundaries. Similar *M-H* loops to those shown in Fig. 12 have been reported for nanotubes fabricated by coating the interior surface of cylindrical pores with cobalt from an organic precursor[18] and Ni nanotubes formed by electrodeposition into surface modified alumina templates.[19]

CONCLUSIONS

We have fabricated Ni nanotubes by etching the Cu core from core/shell Ni–Cu nanowires. The core/shell nanowires are formed by phase separation resulting in a Ni-rich shell and a Cu-rich core. Phase separation is seen in thin films at high Cu(II) concentrations and at more negative deposition potentials. As long as the pore diameter is comparable to smaller than the grain size, single core/shell nanowires are obtained. This finite size effect in nucleation and growth can be exploited for the formation of core/shell nanowires for pore diameters in the range of 100–220 nm.

[1] C. A. Ross, M. Hwang, M. Shima, J. Y. Cheng, M. Farhoud, T. A. Savas, H. I. Smith, W. Schwarzacher, F. M. Ross, M. Redjdal, and F. B. Humphrey, Phys. Rev. B **65**, 144417 (2002).
[2] L. Sun, Y. Hao, C. L. Chien, and P. C. Searson, IBM J. Res. Dev. **49**, 79 (2005).
[3] J. Escrig, P. Landeros, D. Altbir, E. E. Vogel, and P. Vargas, J. Magn. Magn. Mater. **308**, 233 (2007).
[4] F. Q. Zhu, D. L. Fan, X. C. Zhu, J. G. Zhu, R. C. Cammarata, and C. L. Chien, Adv. Mater. (Weinheim, Ger.) **16**, 2155 (2004).
[5] L. Sun, C. L. Chien, and P. C. Searson, Chem. Mater. **16**, 3125 (2004).
[6] T. A. Green, A. E. Russell, and S. Roy, J. Electrochem. Soc. **145**, 875 (1998).
[7] C. C. Yang and H. Y. Cheh, J. Electrochem. Soc. **142**, 3040 (1995).
[8] M. Chen, C. L. Chien, and P. C. Searson, Chem. Mater. **18**, 1595 (2006).
[9] E. Toth-Kadar, L. Peter, T. Becsei, J. Toth, L. Pogany, T. Tarnoczi, P. Kamasa, I. Bakonyi, G. Lang, A. Cziraki, and W. Schwarzacher, J. Electrochem. Soc. **147**, 3311 (2000).
[10] L. Wang, K. Yu Zhang, A. Metrot, P. Bonhomme, and M. Troyon, Thin Solid Films **288**, 86 (1996).
[11] D. M. Tench and J. T. White, J. Electrochem. Soc. **137**, 3061 (1990).
[12] T. P. Moffat, J. Electrochem. Soc. **142**, 3767 (1995).
[13] *Binary Alloy Phase Diagrams* (ASM International, Materials Park, OH, 1996).
[14] C. P. Wang, X. J. Liu, M. Jiang, I. Ohnuma, R. Kainuma, and K. Ishida, J. Phys. Chem. Solids **66**, 256 (2005).
[15] NIST, Joint Committee on Powder Diffraction Standards—International Centre for Diffraction Data (2001).
[16] L. Sun, P. C. Searson, and C. L. Chien, Appl. Phys. Lett. **79**, 4429 (2001).
[17] Z. K. Wang, H. S. Lim, H. Y. Liu, S. C. Ng, M. H. Kuok, L. L. Tay, D. J. Lockwood, M. G. Cottam, K. L. Hobbs, P. R. Larson, J. C. Keay, G. D. Lian, and M. B. Johnson, Phys. Rev. Lett. **94**, 137208 (2005).
[18] K. Nielsch, F. J. Castano, S. Matthias, W. Lee, and C. A. Ross, Adv. Eng. Mater. **7**, 217 (2005).
[19] J. C. Bao, C. Y. Tie, Z. Xu, Q. F. Zhou, D. Shen, and Q. Ma, Adv. Mater. (Weinheim, Ger.) **13**, 1631 (2001).